Lawrence Berkeley National Laboratory

Title
Optimization of PET system design for lesion detection

Permalink
https://escholarship.org/uc/item/7vv8n8t5

Author
Qi, Jinyi

Publication Date
2000-10-13

Optimization of PET System Design for Lesion Detection

Jinyi Qi, *Member, IEEE*

Abstract— **Traditionally, the figures of merit used in designing a PET scanner are spatial resolution, noise equivalent count rate, noise equivalent sensitivity, etc. These measures, however, do not directly reflect the lesion detectability using the PET scanner. Here we propose to optimize PET scanner design directly for lesion detection. The signal-to-noise ratio (SNR) of lesion detection can be easily computed using the theoretical expressions that we have previously derived. Because no time consuming Monte Carlo simulation is needed, the theoretical expressions allow evaluation of a large range of parameters. The PET system parameters can then be chosen to achieve the maximum SNR for lesion detection. The simulation study shown in this paper was focused on a single ring PET scanner without depth of interaction measurement. It can be extended to multi-ring (2D or 3D) PET scanners and detectors with depth of interaction measurement.**

I. INTRODUCTION

Positron emission tomography (PET) is a powerful functional imaging tool in clinical diagnosis and biological research. It has been widely used in detecting and staging cancerous lesions, and PET scanners are under development to acquire high resolution images [1], [2], [3]. Traditionally, the figures of merit used in designing a PET scanner are spatial resolution, noise equivalent count rate, and noise equivalent sensitivity. These measures, however, do not directly reflect the lesion detectability using the PET scanner. Here we propose to optimize PET scanner design directly for lesion detection. Similar idea has been used in optimization of other imaging systems, e.g. [4], [5].

A general method for measuring lesion detectability in medical images is the human observer ROC (receiver operating characteristics) study. This method is very time consuming, and is impossible to carry out in the design phase. As an alternative, computer observers can be used in place of humans. Computer observers not only save time in ROC studies but also provide the possibility of theoretically analyzing the performance of the imaging system. One requirement of analyzing computer observers is the knowledge of the lesion response and noise in reconstructed images. The lesion and noise properties of filtered backprojection (FBP) reconstruction can be computed based on linear transform theory. For statistical reconstruction methods based on the maximum *a posteriori* (MAP) principle (or penalized maximum likelihood), it is more difficult because the algorithms are nonlinear. Recently, progress has been made in this area [6], [7], [8], [9], [10]. Building on this work, we

have derived simplified theoretical expressions for local impulse response and covariance matrix of MAP reconstructions [11], [12] and applied these results to theoretically study the lesion detectability of MAP reconstruction using computer observers [13]. We derived theoretical expressions of the signal-to-noise ratio (SNR) for detecting a known lesion in a known background. These results are useful in comparing algorithms and optimizing system designs. Here we use these results to optimize PET design for lesion detection. MAP reconstruction is used because it can extract more information from PET data than the traditional FBP algorithm [13]. With the development of fast algorithms and increase in computing power, we can expect wide use of MAP reconstruction in resolution-noise critical situations (e.g. early stage cancer detection).

II. THEORY

A. MAP Reconstruction

PET data are well modeled as a collection of independent Poisson random variables, and the appropriate log-likelihood function is given by

$$L(\boldsymbol{y}|\boldsymbol{x}) = \sum_i \left(y_i \log \bar{y}_i - \bar{y}_i - \log y_i! \right) \quad (1)$$

where $\boldsymbol{x} \in I\!\!R^{N \times 1}$ is the unknown image, $\boldsymbol{y} \in I\!\!R^{M \times 1}$ the measured sinogram, and $\bar{\boldsymbol{y}} \in I\!\!R^{M \times 1}$ the mean of the sinogram. The mean sinogram, $\bar{\boldsymbol{y}}$, is related to the image, $\boldsymbol{x}$, through an affine transform

$$\bar{\boldsymbol{y}} = \boldsymbol{P}\boldsymbol{x} + \boldsymbol{s} + \boldsymbol{r} \quad (2)$$

where $\boldsymbol{P} \in I\!\!R^{M \times N}$ is the photon detection probability matrix that models the geometric sensitivity, attenuation, and detector response, and $\boldsymbol{s} \in I\!\!R^{M \times 1}$ and $\boldsymbol{r} \in I\!\!R^{M \times 1}$ are expectations of scatter and randoms in the data, respectively.

A maximum likelihood (ML) estimate of the unknown image can be found as the maximizer of (1). The most popular ML algorithm for PET reconstructions is the expectation maximization (EM) algorithm [14], [15], [16]. However, the ML solution is unstable, as the tomography problem is ill-conditioned. Such problem can be solved by incorporating an image prior in the reconstruction. Most widely used prior functions have a Gibbs distribution form

$$p(\boldsymbol{x}) = \frac{1}{Z} e^{-\beta U(\boldsymbol{x})} \quad (3)$$

where $U(\boldsymbol{x})$ is the energy function, β is the smoothing parameter that controls the resolution of the reconstructed image, and Z is the normalization constant. Here we focus on the quadratic priors, for which the energy function can be expressed as

$$U(\boldsymbol{x}) = \boldsymbol{x}' \boldsymbol{R} \boldsymbol{x}, \quad (4)$$

where $\boldsymbol{R}$ is a positive definite (or semidefinite) matrix.

Combining the likelihood function and the image prior, the MAP reconstruction is found as:

$$\hat{\boldsymbol{x}} = \arg \max_{\boldsymbol{x} \geq 0} \left[L(\boldsymbol{y}|\boldsymbol{x}) - \beta U(\boldsymbol{x}) \right] \qquad (5)$$

Since $L(\boldsymbol{y}|\boldsymbol{x})$ is a concave function of $\boldsymbol{x}$, (5) generally has an unique solution for convex priors.

B. Lesion Detectability

We have studied the lesion detectability of MAP reconstruction using a "signal-known-exactly, background-known-exactly" ROC study with two computer observers: the prewhitening (PW) observer and the non-prewhitening (NPW) observer [13]. Let $\boldsymbol{f}_l$ be the lesion profile and $\boldsymbol{f}_0$ the background image. As we are particularly interested in detection of small lesions, we can assume the lesion is so small that it hardly changes the noise in the data. Thus the noise in $\hat{\boldsymbol{x}}$ is independent of the presence of the lesion. Let $\boldsymbol{h}(\boldsymbol{f}_0 + \boldsymbol{f}_l)$ and $\boldsymbol{h}(\boldsymbol{f}_0)$ denote the mean reconstructions of the image with and without lesion present, respectively. Then the PW observer computes the following test statistic

$$\eta_{\mathrm{PW}}(\hat{\boldsymbol{x}}) = [\boldsymbol{h}(\boldsymbol{f}_0 + \boldsymbol{f}_l) - \boldsymbol{h}(\boldsymbol{f}_0)]' \boldsymbol{\Sigma}^{-1} \hat{\boldsymbol{x}}, \qquad (6)$$

where $\boldsymbol{\Sigma}$ is the ensemble covariance matrix of $\hat{\boldsymbol{x}}$. A decision whether there is a lesion or not is then made by comparing this statistic to a pre-selected threshold. If $\eta(\hat{\boldsymbol{x}})$ exceeds the decision threshold, $\hat{\boldsymbol{x}}$ is determined to have a lesion. Otherwise, it is not.

The performance of the PW observer can be measured by the SNR defined as

$$
\begin{aligned}
\mathrm{SNR}^2_{\mathrm{PW}} &= \frac{\{\eta_{\mathrm{PW}}[\boldsymbol{h}(\boldsymbol{f}_0 + \boldsymbol{f}_l)] - \eta_{\mathrm{PW}}[\boldsymbol{h}(\boldsymbol{f}_0)]\}^2}{\mathrm{var}[\eta_{\mathrm{PW}}(\hat{\boldsymbol{x}})]} \\
&= \boldsymbol{z}' \boldsymbol{\Sigma}^{-1} \boldsymbol{z},
\end{aligned}
\qquad (7)
$$

where $\boldsymbol{z} \equiv \boldsymbol{h}(\boldsymbol{f}_0 + \boldsymbol{f}_l) - \boldsymbol{h}(\boldsymbol{f}_0)$. When $\eta_{\mathrm{PW}}(\hat{\boldsymbol{x}})$ is normally distributed, the SNR is related to the area under the ROC curve by the error function [17]. Therefore, we use the SNR as the measure of lesion detectability.

Using the first order Taylor series approximation, $\boldsymbol{z}$ can be expressed as a convolution between the lesion profile $\boldsymbol{f}_l$ and the local impulse response function at the lesion location. Building on the previous results of approximations of the local impulse function and covariance matrix [7], [8], [12], we have derived in [13] that

$$\mathrm{SNR}^2_{\mathrm{PW}} \approx \boldsymbol{f}_l' \boldsymbol{P}' \mathrm{diag}\left[\frac{1}{\bar{y}_i}\right] \boldsymbol{P} \boldsymbol{f}_l, \qquad (8)$$

where $\mathrm{diag}\left[\frac{1}{\bar{y}_i}\right]$ denotes a diagonal matrix with the (i,i)th element equal to $\frac{1}{\bar{y}_i}$.

The PW observer gives the optimal performance on lesion detection, when $\hat{\boldsymbol{x}}$ is normally distributed. We have shown in [12] that the distributions of voxel values in MAP reconstructions can be approximated by normal distributions in regions where the activity is not very low. Therefore, the PW observer gives an upper bound of lesion detectability that is achievable when
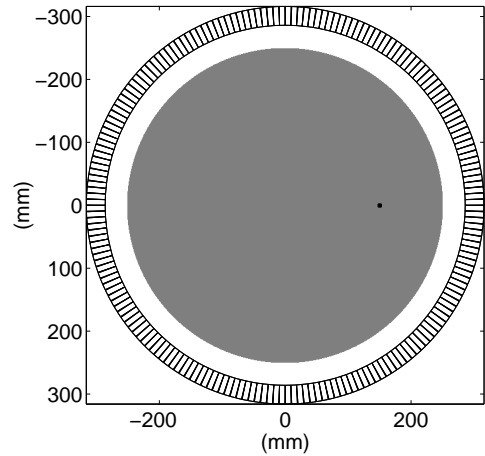

Fig. 1. Configuration of the PET system simulation. The background activity is a uniform cylindrical source; the lesion is also a uniform cylindrical source with much smaller diameter. The activity ratio between the lesion and the background is 2:1. The detectors are closely packed with no dead space between each other.

all the information is used. In general, however, humans are incapable of prewhitening the noise in the image [18]. This has led to using the NPW or other observer for predicting human performance. The NPW observer uses a simple matched filter to compute the test statistic

$$\eta_{\mathrm{NPW}}(\hat{\boldsymbol{x}}) = [\boldsymbol{h}(\boldsymbol{f}_0 + \boldsymbol{f}_l) - \boldsymbol{h}(\boldsymbol{f}_0)]' \hat{\boldsymbol{x}}. \qquad (9)$$

Eq. (9) differs from (6) only by deletion of $\boldsymbol{\Sigma}^{-1}$ that accounts for the prewhitening operation. Similarly, we have also derived simplified expression for SNR of NPW observer [13]

$$
\begin{aligned}
\mathrm{SNR}^2_{\mathrm{NPW}} &\approx \left(\sum_i \left(\frac{\lambda_i(j)\zeta_i}{\lambda_i(j) + \beta\mu_i} \right)^2 \right)^2 \\
&\times \left(N \sum_i \frac{\lambda_i^3(j)\zeta_i^2}{(\lambda_i(j) + \beta\mu_i)^4} \right)^{-1}, \quad (10)
\end{aligned}
$$

where $\{\lambda_i(j),\ i = 1, \ldots, N\}$ is the Fourier transform of the locally shift invariant approximation of $\boldsymbol{P}' D[\bar{y}_i^{-1}]\boldsymbol{P}$ at the lesion location, $\{\mu_i,\ i = 1, \ldots, N\}$ is the Fourier transform of $\boldsymbol{R}$, and $\{\zeta_i,\ i = 1, \ldots, N\}$ is the Fourier transform of the lesion profile $\boldsymbol{f}_l$.

III. PET SYSTEM DESIGN

In this section, we study the performance in lesion detection of a single ring PET system. In spite of the difference between PW and NPW observer, we have found in [13] that for the imaging algorithm that has greater $\mathrm{SNR}_{\mathrm{PW}}$, the $\mathrm{SNR}_{\mathrm{NPW}}$ is also greater. As a result, we here only use the $\mathrm{SNR}_{\mathrm{PW}}$ in (8) as the measure of PET system performance. The background was a uniform activity cylindrical source and the lesion was also a uniform cylindrical source with much smaller diameter. The configuration of the simulated PET system is illustrated in Fig. 1.

In the simulations, each crystal was treated as an individual detector with no dead space between each other. The sinograms were calculated analytically with modeling of depth-dependent
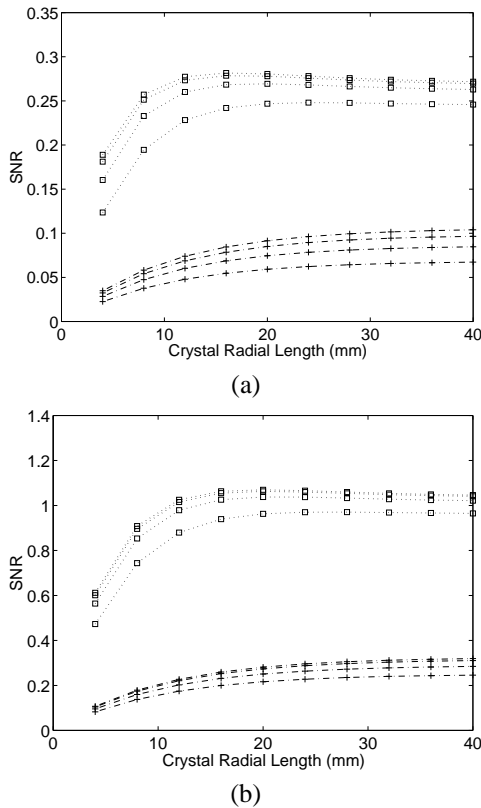
(a)

(b)

Fig. 2. SNR for detecting a round lesion at two different radial locations inside a 50cm diameter uniform background. The diameter of the lesion is (a) 2mm and (b) 4mm. The "+"s correspond to the lesion at center and the squares correspond to the lesion at radial offset of 24cm. The curves for each lesion, from top to bottom, correspond to detector size of 1.13mm, 2.25mm, 4.50mm, and 9.0mm, respectively.
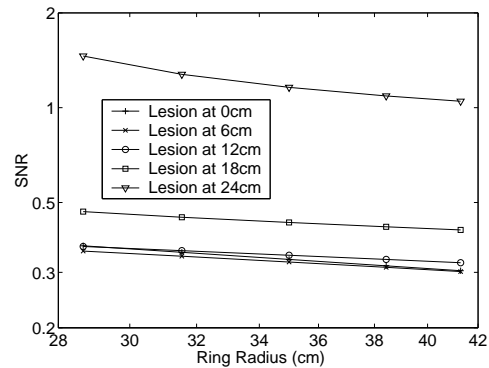

Fig. 3. SNR of detecting a 4mm lesion at different radial locations in a 50cm diameter uniform background as a function of detector ring diameter. The total number of true events is 1M when ring radius is 41.3cm.

solid angle, object self-attenuation and crystal penetration effects. The attenuation coefficients of the object and detector crystal were 0.01mm^{-1} and 0.1mm^{-1}, respectively. The detector positioning error was simulated using a Gaussian blurring function with FWHM of 1.5mm. Other physical effects, such as positron range, photon non-collinearity, detector energy resolution, are ignored.

The parameters that we studied here are detector ring diameter, crystal transaxial width, and crystal radial length. They are studied with different size of the background and lesion. For all the configurations, the axial crystal size is considered as fixed and independent of the transaxial width. We will first ignore randoms and scatters in the data, and will return to them in Section III-D.

A. Whole Body Scanner

To simulate whole body scan situation, we set the background diameter to 50cm. The scanner ring diameter was varied from 82.5cm to 57cm, where the largest one is similar to that of a EXACT HR+ scanner (CTI PET system, Knoxville, TN). The detector transaxial sizes were 1.13mm, 2.25mm, 4.50mm, and 9.0mm. The radial length of detector crystal was varied from 4mm to 40mm.

In Fig. 2 we plot the SNR for detecting a 2mm and a 4mm diameter round lesions each at two different radial locations: ra-

dial center and radial offset of 24cm. The activity ratio between the lesion and the background was 2:1. The mean of total number of detections was 1M. The PET ring diameter in this case was 82.5cm. The plots look similar for all the other ring diameters that we studied, although the absolute SNR values are different. Eq. (8) shows that SNR is linearly proportional to the contrast of the lesion, and to the square root of total count, so the SNR curves for lesions with different contrast and different count level can be easily generated from Fig. 2.

Clearly, the SNR is much higher for detecting a lesion at boundary than for a lesion at radial center because of the photon attenuation. For the center lesion, the SNR monotonically increase as a function of crystal radial length with all detector sizes. For the radial off-center lesion, however, the SNR reaches the maximum at a certain length of crystal because of the stronger crystal penetration effect for longer crystals. The optimum crystal length is dependent on the detector size and lesion size. The larger the detector size or lesion size, the longer the optimum crystal length. We also found that the smaller the ring diameter, the shorter the optimum crystal length.

For all lesion locations, we found that SNR increases as detector transaxial size decreases, while the improvement of SNR becomes less as the detector size becomes smaller. With consideration of the cost of manufacturing small detectors and the dead space between crystals, the optimum detector size is about half of or equal to the targeted lesion size.

In Fig. 3, we plot the SNR for detecting a 4mm lesion at different radial locations as a function of detector ring diameter. Here the detector transaxial size was 2.25mm, and radial length was 32mm. The plots for all the other situations look similar. It shows that the SNR monotonically increases as the ring diameter decreases in the absence of randoms and scatters. For the center lesion, the SNR is inversely proportional to the square root of the ring diameter, while for the lesion at 24cm radial offset, the rate is greater. This indicates that to achieve highest SNR for lesion detection in the absence of randoms and scatters, we need to build PET scanner with smallest ring diameter as possible provided that we accurately model the photon detection process.
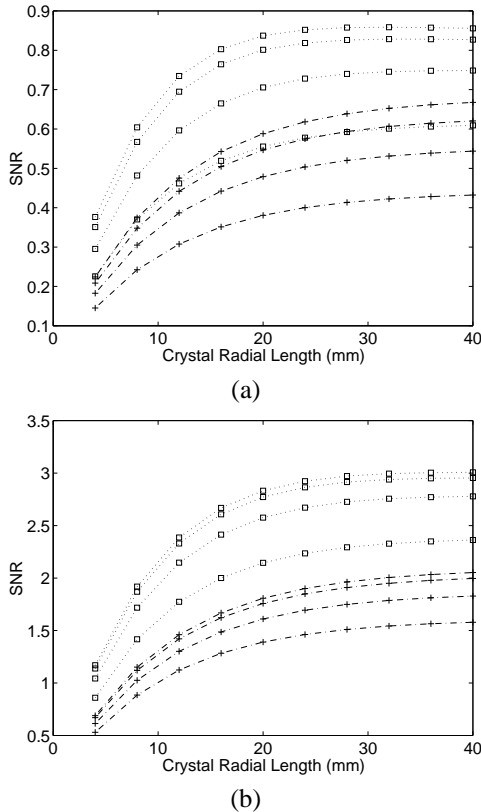
(a)

(b)

Fig. 4. SNR for detecting a round lesion at two different radial locations inside a 20cm diameter uniform background. The diameter of the lesion is (a) 2mm and (b) 4mm. The "+"s correspond to the lesion at center and the squares correspond to the lesion at radial offset of 9cm. The curves for each lesion, from top to bottom, correspond to detector size of 1.13mm, 2.25mm, 4.50mm, and 9.0mm, respectively.

B. Brain Scanner

For brain scanner simulations, we set the background diameter to 20cm. The ring diameter was varied from 82.5cm to 26cm. The detector transaxial size and radial length were in the same range as those for whole body scanner in Section III-A.

In Fig. 4 we plot the SNR for detecting a 2mm and a 4mm diameter round lesions each at two different radial locations: radial center and radial offset of 9cm. The activity ratio, total number of detections, and the PET ring diameter were the same as those in Fig. 2. Again, the SNR is higher for detecting a lesion at boundary than for a lesion at radial center because of the photon attenuation, but the difference is less than that of the whole body scanner because the attenuation for the center lesion is smaller. Except for case of the 2mm lesion at boundary with 1.13mm detector size, the SNR increases monotonically as crystal radial length increases with all transaxial detector sizes. Unlike the whole body scanner, the optimum crystal length appears to be 40mm for the lesion larger than 2mm in diameter at all locations. The similar relationship holds for all other ring diameters that we studied.

For all lesion locations, the SNR also increases as detector transaxial size decreases, which is the same as that in whole body scanner.

In Fig. 5, we plot the SNR for detecting a 2mm lesion at different radial locations as a function of detector ring diameter.
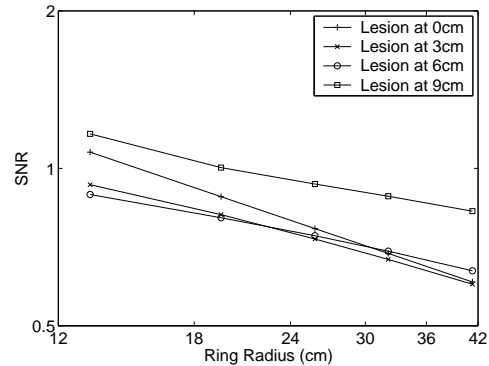

Fig. 5. SNR of detecting a 2mm lesion at different radial locations as a function of detector ring diameter in a 20cm diameter uniform background.

The detector transaxial size and radial length were the same as those in Fig. 3. Again, the SNR monotonically increases as the ring diameter decreases in the absence of randoms and scatters.

C. Small Animal Scanner

There has been great interest in building PET scanner dedicated for small animal imaging. These small animal scanners have higher resolution and sensitivity than the human scanners. We simulated such small animal scanner by setting the background diameter to 10cm and varying the ring diameter from 17.2cm to 11.5cm. The detector transaxial sizes were .5mm, 1.0mm, 2.0mm, and 4.0mm. The radial length was varied from 4mm to 40mm. For reference, the microPET scanner [1] has ring diameter of 17.2cm and detector size of 2.0mm (transaxial) × 10mm (radial).

Fig. 6 shows the plots of SNR for detecting a 1mm and a 3mm diameter round lesions each at two different radial locations: radial center and radial offset of 45mm. The activity ratio between the lesion and the background was 2:1; the total number of detections was 1M; and the PET ring diameter was 17.2cm.

Unlike the whole body or brain situation, the SNR of the 1mm lesion at center is greater than that of the same lesion at 4.5cm radial offset (or is close to for the 3mm lesion). This is due to the reduced attenuation for the center location in a small object. Similar to the brain scanner, SNR increases monotonically as crystal radial length increases with the optimum crystal length to be 40mm. The SNR also increases as detector transaxial size decreases, which is the same as that in whole body and brain scanners.

Fig. 7 shows the plots of SNR for detecting a 1mm lesion at different radial locations as a function of detector ring diameter. The detector transaxial size was 1mm and radial length was 32mm. Again, the SNR monotonically increases as the ring diameter decreases in the absence of randoms and scatters.

D. Effects of Randoms and Scatters

In the above simulations, we have been ignoring randoms and scatters. Here we examine some of their effects on PET design. For simplicity, we used the simple random and scatter model derived in [19]. The model assumes the source activity is concentrated along the axis of the scanner. We further assumed that the random sinogram and scatter sinogram are uniform. Al-
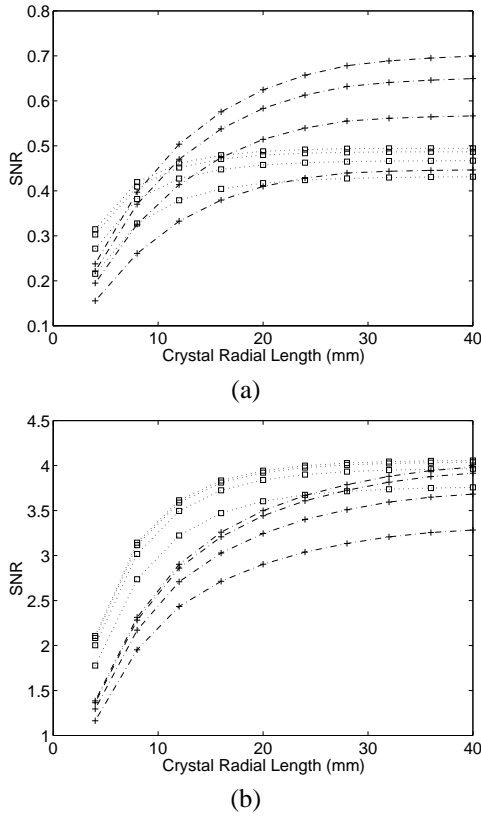
(a)

(b)

Fig. 6. SNR for detecting a round lesion at two different radial locations inside a 10cm diameter uniform background. The diameter of the lesion is (a) 1mm and (b) 3mm. The "+"s correspond to the lesion at center and the squares correspond to the lesion at radial offset of 4.5cm. The curves for each lesion, from top to bottom, correspond to detector size of .5mm, 1.0mm, 2.0mm, and 4.0mm, respectively.

(a)

(b)

Fig. 8. SNR for detecting a 4mm lesion at the center of a whole body scanner as a function of detector ring diameter with different level of randoms and scatters: (a) without out-of-FOV activity; (b) with out-of-FOV activity. The random and scatter levels of each curve are, from top to bottom, 0%, 5%, 10%, and 20% of the true events, respectively, when the ring radius is 41.3cm.
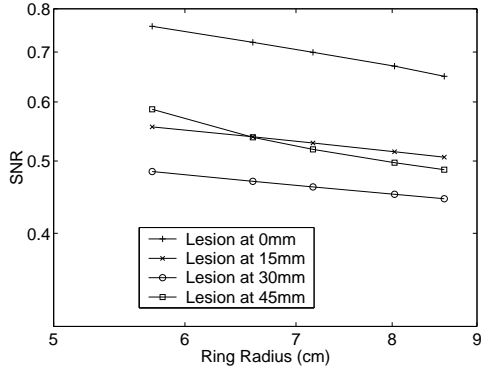

Fig. 7. SNR of detecting a 1mm lesion at different radial locations as a function of detector ring diameter in a 10cm diameter uniform background.

though these assumptions do not strictly hold here, nonetheless, this simple model can provide us some insight on the effects of randoms and scatters.

As shown in (2) and (8), the expectations of randoms and scatters appear in the denominator in the diagonal matrix. Hence, the SNR decreases as randoms and scatters increase. For the simplified system that was studied here, we assumed that the fraction of randoms and scatters is independent of the crystal length and crystal size, and focused on the change of randoms and scatters as a function of ring diameter. When the ring di-
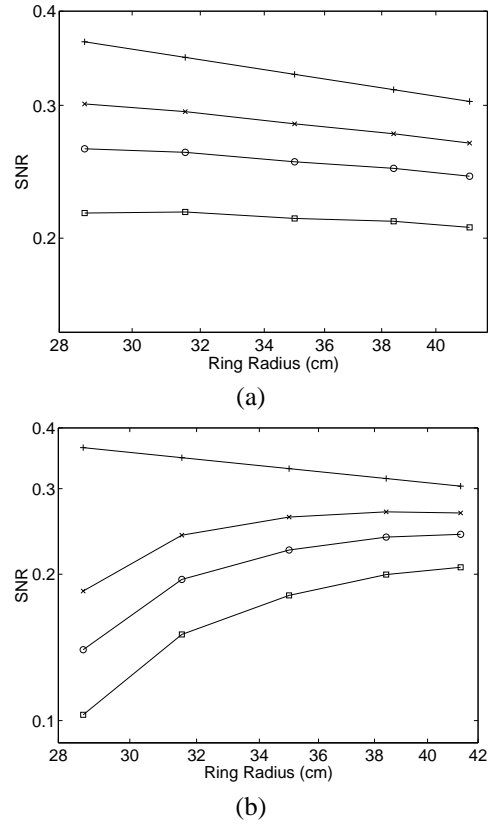
ameter is reduced, the randoms and scatters will be increased by the following two factors: (i) increased solid angle; (ii) reduced side shielding that blocks out-of-FOV photons.

Firstly let us consider the situation where all activity is inside the FOV. In this case, the fraction of randoms and scatters is solely affected by the change of the solid angle. The total number of true events is roughly proportional to $1/d$, while the total numbers of randoms and scatters are roughly proportional to $1/d^2$, where d is the diameter of the PET detector ring. Fig. 8(a) shows the plots of SNR for detecting a 4mm lesion at the center of a whole body scanner as a function of detector ring diameter with different level of randoms and scatters. The PET system configurations were the same as those of Fig. 3. Fig. 8(a) shows that as the random and scatter levels increase, the PET system with smaller ring diameter become less and less appealing because the increase in sensitivity is more and more offset by the increase in randoms and scatters.

Secondly we study the effect of the out-of-FOV activity. In order to reduce the events from out-of-FOV activity, the PET system should be built with the maximum amount of side shielding, where the lead shielding extends from the detector ring to the patient port. For a fixed size patient port, the smaller the ring diameter, the less the side shielding (and hence more randoms and scatters from the outside). From the results in [19], we obtained the following approximate formulae for the total number

of detections:

$$\text{Trues} \quad \propto \quad \frac{1}{d} \tag{11}$$

$$\text{Scatters} \quad \propto \quad \frac{1}{(d-p)d} \tag{12}$$

$$\text{Randoms} \quad \propto \quad \frac{1}{(d-p)^2} \tag{13}$$

where p is the diameter of the patient port. These formulae assume that the activity is concentrated along the axis of the scanner and is very long. They are less accurate when $d - p$ is small.

Fig. 8(b) shows the plots of SNR for detecting the same lesion as that of Fig. 8(a) with out-of-FOV activity. Here we set the patient port to be the same size as the background disk ($p = 50\text{cm}$). By comparison, the SNR of the PET system with smaller ring diameter drops much faster in Fig. 8(b) as the random and scatter levels increase because of the out-of-FOV activity.

Therefore, when designing a PET system, if the anticipated random and scatter levels are low and there is no out-of-FOV activity, a small ring diameter may help lesion detection by increasing sensitivity; otherwise, it is better to have large ring diameter and large side shielding to reduce randoms and scatters.

IV. CONCLUSION AND DISCUSSION

We have developed an approach for optimizing PET system design for lesion detection. The SNR of lesion detection can be easily computed using the theoretical expressions that we have previously derived. Because no time consuming Monte Carlo simulation is needed, the theoretical expressions allow evaluation of a large range of parameters. The PET system parameters can then be chosen to achieve the maximum SNR for lesion detection.

In this paper, we have studied a single ring PET scanner. The parameters are ring diameter, detector transaxial size and radial length. The results show that (i) the optimum ring diameter depends on the random and scatter levels: when the random and scatter levels are very low, the SNR of lesion detection increases as the ring diameter decreases; when random and scatter levels are high, especially with out-of-FOV activity, large ring diameter with large side shielding is better. (ii) The optimum detector transaxial size is the smallest possible. However, this would not be true if the dead space between detectors is significant compared to the size of the detectors. (iii) The optimum detector radial length depends on the crystal material, the size and location of the target lesion, and the size of the background. We can either optimize the crystal length for a target lesion based on the specific PET application, or optimize the average SNR for a range of lesion sizes and locations.

In the analysis, we used the "signal-known-exactly, background-known-exactly" observer task. This is a highly simplified scenario compared to real clinical detection tasks. More realistic modeling of the lesion and background will be helpful in improving the method. In addition, we have not modeled any error in the detection probability matrix $\boldsymbol{P}$ and the expectations of randoms and scatters, i.e. we assumed that the forward model (2) is exact. However, in the real world there are always errors in the model. A more ill-conditioned system is more susceptible to the errors in the model. Therefore, when such errors are large, they will have some impact on the results. We plan to study these issues and extend the method to 3D scanners in future work.

REFERENCES

[1] S. R. Cherry, Y. Shao, S. Siegel, R. W. Silverman, K. Meadors, J. Young, W. F. Jones, D. Newport, C. Moyers, E. Mumcuoglu, M. Andreaco, M. Paulus, D. Binkley, R. Nutt, and M. E. Phelps, "MicroPET: A high resolution PET scanner for imaging small animals," *IEEE Transactions on Nuclear Science*, vol. 44, pp. 1161–1166, 1997.

[2] W. Moses, P. Virador, S. Derenzo, R. Huesman, and T. Budinger, "Design of a high-resolution, high-sensitivity PET camera for human brains and small animals," *IEEE Transactions on Nuclear Science*, vol. 44, pp. 1487–1491, 1997.

[3] M. Schmand, K. Wienhard, M. Casey, et al., "Performance evaluation of a new LSO high resolution research tomograph - HRRT," in *Proceedings of IEEE Nuclear Science Symposium and Medical Imaging Conference*, Seattle, WA, 1999.

[4] W. E. Smith and H. H. Barrett, "Hotelling trace criterion as a figure of merit for the optimization of imaging systems," *Journal of the Optical Society of America A*, vol. 3, pp. 717–725, 1986.

[5] R. D. Fiete, H. H. Barrett, W. E. Smith, and K. J. Myers, "Hotelling trace criterion and its correlation with human-observer performance," *Journal of the Optical Society of America A*, vol. 4, pp. 945–953, 1987.

[6] H. H. Barrett, D. W. Wilson, and B. M. W. Tsui, "Noise properties of the EM algorithm: I. theory," *Physics in Medicine and Biology*, vol. 39, pp. 833–846, 1994.

[7] J. A. Fessler, "Mean and variance of implicitly defined biased estimators (such as penalized maximum likelihood): Applications to tomography," *IEEE Transactions on Image Processing*, vol. 5, pp. 493–506, 1996.

[8] J. A. Fessler and W. L. Rogers, "Spatial resolution properties of penalized-likelihood image reconstruction: Spatial-invariant tomographs," *IEEE Transactions on Image Processing*, vol. 9, pp. 1346–1358, 1996.

[9] W. Wang and G. Gindi, "Noise analysis of MAP-EM algorithms for emission tomography," *Physics in Medicine and Biology*, vol. 42, pp. 2215–2232, 1997.

[10] E. J. Soares, C. L. Byrne, and S. J. Glick, "Noise characterization of block-iterative reconstruction algorithms: I. theory," *IEEE Transactions on Medical Imaging*, vol. 19, pp. 261–270, 2000.

[11] J. Qi and R. M. Leahy, "A theoretical study of the contrast recovery and variance of MAP reconstructions from PET data," *IEEE Transactions on Medical Imaging*, vol. 18, pp. 293–305, 1999.

[12] J. Qi and R. M. Leahy, "Resolution and noise properties of MAP reconstruction for fully 3D PET," *IEEE Transactions on Medical Imaging*, vol. 19, pp. 493–506, 2000.

[13] J. Qi and R. H. Huesman, "Theoretical study of lesion detectability of MAP reconstruction using computer observers," *IEEE Transactions on Medical Imaging*, vol. 20, 2001, to appear.

[14] A. Dempster, N. Laird, and D. Rubin, "Maximum likelihood from incomplete data via the EM algorithm," *Journal of Royal Statistical Society, Series B*, vol. 39, pp. 1–38, 1977.

[15] L. Shepp and Y. Vardi, "Maximum likelihood reconstruction for emission tomography," *IEEE Transactions on Medical Imaging*, vol. 1, pp. 113–122, 1982.

[16] K. Lange and R. Carson, "EM reconstruction algorithms for emission and transmission tomography," *Journal of Computer Assisted Tomography*, vol. 8, pp. 306–316, 1984.

[17] H. H. Barrett, T. Gooley, K. Girodias, J. Rolland, T. White, and J. Yao, "Linear discriminants and image quality," *Image and Vision Computing*, vol. 10, pp. 451–460, 1992.

[18] K. J. Myers, H. H. Barrett, M. C. Borgstrom, D. D. Patton, and G. W. Seeley, "Effect of noise correlation on detectability of disk signals in medical imaging," *Journal of the Optical Society of America A*, vol. 2, pp. 1752–1759, 1985.

[19] S. E. Derenzo, H. Zaklad, and T. F. Budinger, "Analytical study of a high-resolution positron ring detector system for transaxial reconstruction tomography," *Journal of Nuclear Medicine*, vol. 16, pp. 1166–1173, 1975.